npj | flexible electronics

Article

Published in partnership with Nanjing Tech University

https://doi.org/10.1038/s41528-026-00541-9

Phytic acid-assisted low-temperature carbonization of jute fabric for high-performance flexible pressure sensors

Bo xuan Zhu[1], Lu wen Zhao[1], Li Lv[1], Cheng cheng Li[1], Miao Zhang[1], Jie Wang[1], Xing Su[2], Zai sheng Cai[1] & Ya ping Zhao[1] ✉

Carbon materials are ideal for flexible pressure sensors owing to their stable conductivity and light weight, yet conventional carbonization often sacrifices flexibility for electrical performance. Here, we report a phytic acid (PA)-assisted strategy that lowers the carbonization temperature of jute by 200 °C while markedly enhancing mechanical properties—showing a 24.9-fold increase in fracture strength (reaching 91.50 kPa), improved elongation (17.96%), and low sheet resistance (8.48 ± 0.45 Ω/sq). We have developed a flexible pressure sensor (TPU/CPA/DJ) by combining four-layer phytate-assisted carbonated degummed jute (CPA/DJ) with thermoplastic polyurethane (TPU) via solvent-induced phase separation technology. The sensor exhibits high sensitivity (5.28 kPa^{-1}), a broad detection range (5 Pa to 200 kPa), and a fast response time. The device reliably monitors both human motion and subtle pressures. This work elucidates the role of phosphorus-catalyzed carbon layer formation during low-temperature conversion and provides a sustainable route to high-performance wearable electronics.

Recent advances in electronic technologies have accelerated the development of flexible wearable pressure sensors, meeting growing demands for high-quality lifestyle and personalized health monitoring[1–4]. These sensors are critical in applications such as continuous physiological tracking, human-machine interfaces, and smart consumer electronics, where high sensitivity, accuracy, flexibility, biocompatibility, and long-term stability are essential[5–10].

The performance of flexible sensors strongly depends on the choice of active materials[10–13]. Commonly used systems include carbon-based nanomaterials[14–17], metallic nanostructures[18–21], functional composites[22–24], and inorganic semiconductors[25–27]. Among these, carbon-based materials are especially promising due to their superior electrical conductivity, excellent stability, high charge mobility, and light weight[28–31]. Biomass-derived carbons offer additional advantages in sustainability, cost-effectiveness, and environmental friendliness. However, traditional high-temperature carbonization often degrades the mechanical flexibility and strength of natural fibers. Recent modifications, such as $V_2O_5/ZnCl_2$-treated cotton[32] and phosphate-stabilized cellulose fibers[33], demonstrate that tailored treatments can preserve key functional properties.

Nevertheless, the high carbonization temperatures (>700 °C) typically required for biomass-based carbons raise concerns regarding safety, energy consumption, and material integrity. Flame-retardant treatments have shown promise in reducing carbonization temperatures while enhancing carbon yield and structural stability. Phosphorus and nitrogen-based flame retardants play a critical role in enabling low-temperature carbonization by promoting dehydration and char formation, as evidenced by their ability to significantly reduce decomposition temperatures, enhance carbon layer density, and improve carbon yield in various biomass treatments[34–36].

Jute, a natural fiber with high cellulose content (53–70%) and an innate hierarchical pore structure, serves as an excellent precursor for carbon-based sensing materials. Its structural properties facilitate the synthesis of high-surface-area activated carbon (470–541.9 $m^2 g^{-1}$)[37]. which can be further optimized to tailor pore size distribution and achieve pore volumes up to 0.232 $cm^3 g^{-1}$[38]. Carbonization yields a porous architecture that establishes an efficient conductive network for electron transport and enhances strain-responsive behavior, rendering it particularly suitable for high-performance sensing applications. Moreover, the utilization of jute waste aligns with circular economy principles by offering a sustainable pathway for electronic device fabrication. To overcome the inherent brittleness of carbonized textiles, polymer reinforcements like TPU have been employed. Zhang et al.[39] developed a a freeze-casted porous TPU sensor with broad detection range (0–1.2 MPa), fast response (140 ms), and durability (>3000 cycles). Similarly, He et al.[40] fabricated a TPU-reinforced carbonized wood aerogel sensor exhibiting 90% compressibility, a sensitivity of 76.18 kPa^{-1}, and stability over 10,000 cycles. These findings indicate that polymer integration plays an essential role in enhancing the elasticity and durability of carbon-based sensing materials.

[1]College of Chemistry and Chemical Engineering, Donghua University, Shanghai, China. [2]School of Energy and Environment, Southeast University, Nanjing, China. ✉e-mail: zhaoyping@dhu.edu.cn

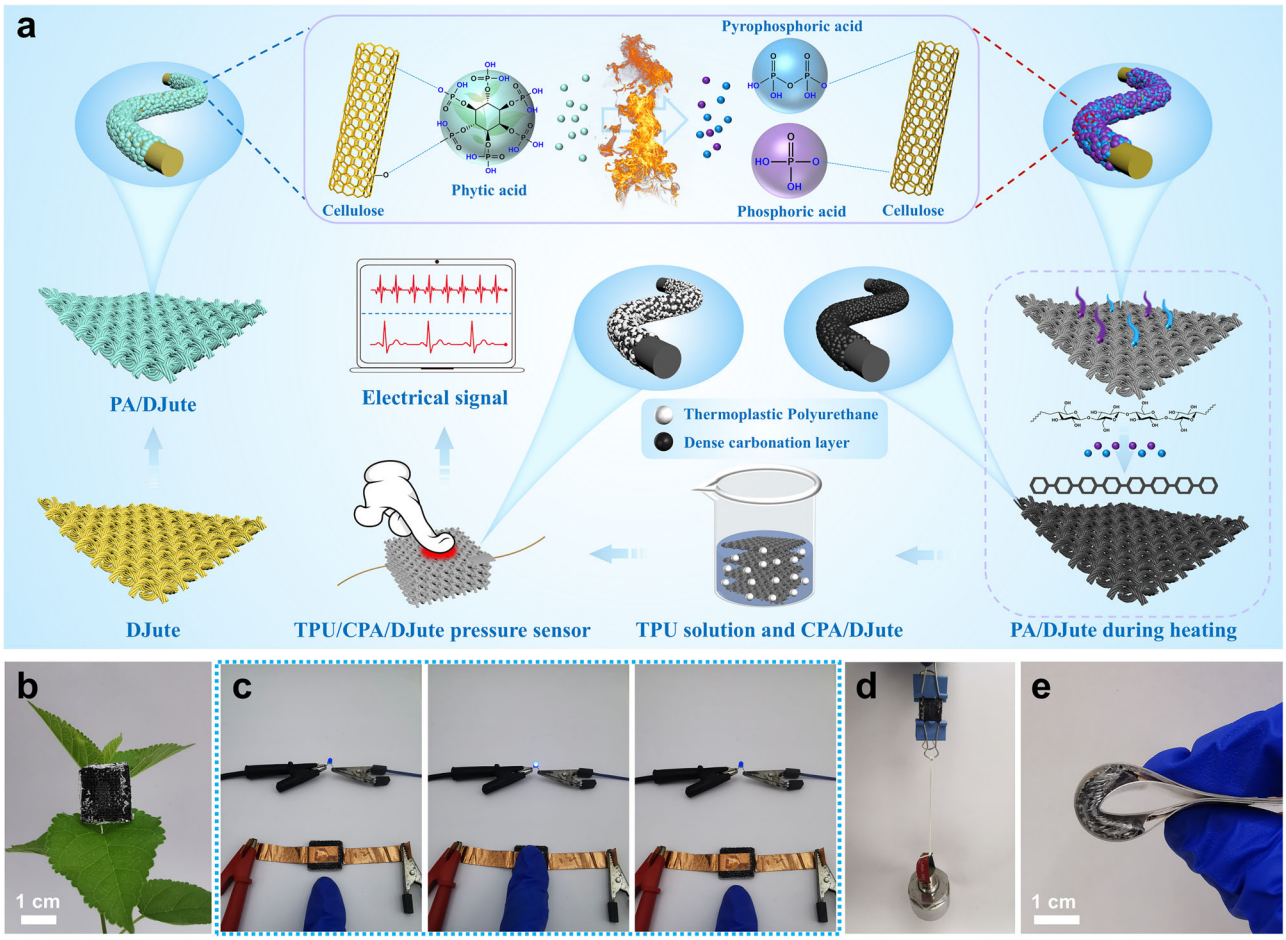

Fig. 1 | Preparation process and fundamental physical properties of TPU/CPA/DJ sensors. a Schematic of the multilayer-assembled TPU/CPA/DJ flexible pressure sensor fabrication process. **b** Optical image demonstrating ultra-lightweight properties (density: 0.12 g/cm^3), where the sensor adheres to a leaf surface without slippage or deformation. **c** Brightness change of LEDs during finger pressure loading and unloading. **d** Optical image of a sample stretched longitudinally with a 200 g hydrothermal reactor cap. **e** Optical picture of the sample when folded in half.

This study develops a multilayer flexible pressure sensor based on phytic acid-assisted carbonized waste degummed jute fabrics (CPA/DJ), encapsulated with thermoplastic polyurethane (TPU). The fabrication process includes degumming, flame-retardant functionalization, oxidation, carbonization, and TPU integration. Phytic acid (PA) treatment significantly reduces the carbonization temperature while simultaneously enhancing mechanical properties. The constructed sensor (TPU/CPA/DJ) exhibits high sensitivity, a wide detection range, and an ultralow detection limit, enabling real-time monitoring of both human physiological activities and subtle environmental pressures. This work establishes a flame-retardant-assisted low-temperature carbonization strategy and promotes the development of sustainable, high-performance wearable sensors from natural fiber sources.

Results

Preparation process and design concept of TPU/CPA/DJ

Figure 1a schematically illustrates the fabrication process of the TPU/CPA/DJ flexible pressure sensor, wherein PA, a phosphorus-rich biogenic compound, serves as a catalytic agent to enable low-temperature carbonization (500 °C) of jute fabric. When treating jute fabrics with PA solution, the hydrophobic gum on the fabric surface prevents the PA solution from quickly soaking into the fabric, which isn't great for PA adhesion. Following degumming, the hydrophilicity of jute fabric is markedly enhanced, facilitating uniform PA adhesion (Supplementary Fig. S1). During thermal treatment, PA decomposes into acidic compounds (e.g., $H_4P_2O_7$, H_3PO_4) at 200–300 °C (Supplementary Fig. S2a, b)[41]. These acids subsequently catalyze fabric dehydration and cross-linking between 300 °C and 400 °C, driving controlled aromatization to form a nascent char (Supplementary Fig. S2a, c)[34]. Above 400 °C, the acidic products further promote the decomposition, reorganization, and crystallization of this char, leading to the formation of a dense, protective carbonized layer on the fabric surface at a reduced temperature (Supplementary Fig. S2a, d)[42]. Consequently, PA treatment significantly lowers the conventional carbonization temperature while helping preserve the fabric's specific mechanical strength.

The carbonized fabric was encapsulated with TPU to construct the pressure sensor, with detailed methodology provided in the Experimental Section. Remarkably, the sensor exhibits ultra-lightweight characteristics (<0.15 g/cm^3), demonstrated by its ability to be supported on a flat green leaf without causing deformation (Fig. 1b), highlighting its suitability for minimally invasive wearable applications. The sensor has excellent sensitivity, flexibility, resilience, and mechanical properties, which provide a solid foundation for it to be made into a wearable flexible pressure sensor. The electromechanical performance was verified by a simple circuit in which a finger pressure-triggered resistance change induced visible LED brightness modulation (Fig. 1c). The sensor can easily pull up an object of 200 g (Fig. 1d) and bend it arbitrarily (Fig. 1e), which shows that the sensor maintains its original form when subjected to lateral force, retains the application effect, and has good mechanical strength and flexibility.

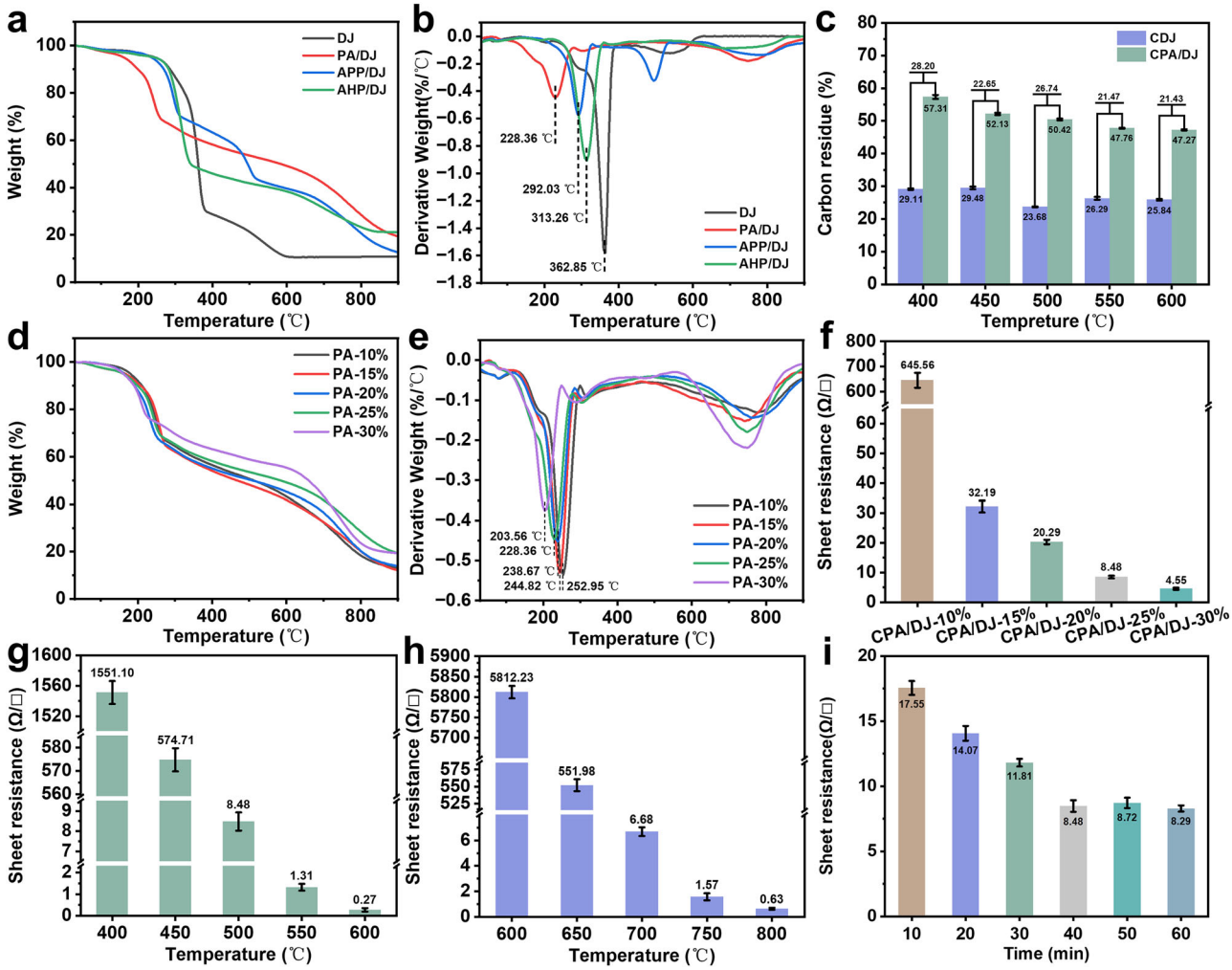

Fig. 2 | Mechanistic study and process optimization for jute fabric carbonization. **a**, **b** Thermogravimetry (TG) and derivative thermogravimetry (DTG) curves of DJ and DJ treated with various flame retardants, respectively. **c** Carbon yield of DJ and phytate-treated jute fabrics at different carbonization temperatures. **d**, **e** TG and DTG curves of jute fabrics treated with different concentrations of PA, respectively. **f** Sheet resistance of carbonized jute versus PA concentration (10–30 wt%). Sheet resistance of PA-treated jute (**g**) and degummed jute (**h**) as a function of carbonization temperature. **i** Sheet resistance of jute fabrics after PA treatment with different carbonization times.

Mechanistic study and process optimization for jute fabric carbonization

Upon thermal activation, PA decomposes into acidic species (e.g., pyrophosphoric acid and phosphoric acid), catalyzing the formation of compact carbonaceous char layers on fabric surfaces at much lower temperatures[43]. These thermally stable char layers inhibit heat and mass transfer via condensed-phase flame retardancy mechanisms, suppressing fabric combustion[44], thus providing a new pathway for low-temperature char formation in cellulosic materials. To evaluate this mechanism, a phosphorous-based flame retardant comprising PA, ammonium polyphosphate (APP), and aluminum hypophosphite (AHP) was applied to jute fabric at a 25% mass fraction concentration via a soak-pad-dry process. TGA under nitrogen (20 mL/min) showed significant differences in thermal degradation between treated fabrics and untreated degummed jute (DJ) (Fig. 2a).

Flame-retardant treatments reduced the maximum thermal decomposition temperature (T_{max}) substantially. Phytic acid-loaded degummed jute fabric (PA/DJ) had the most significant effect, with T_{max} = 134.49 °C lower than untreated DJ ($p < 0.01$). Ammonium polyphosphate-loaded degummed jute fabric (APP/DJ) and aluminum hypophosphite-loaded degummed jute fabric (AHP/DJ) showed reductions of 70.82 °C (292.03 ± 1.2 °C) and 49.59 °C (313.26 ± 1.5 °C) respectively (Fig. 2b). Their temperature-lowering efficiency followed PA > APP > AHP, consistent with previous reports on phosphorus catalysis in cellulose pyrolysis[45–47]. Char yield of PA/DJ improved significantly at 400–600 °C: 28.20% (400 °C), 22.65% (450 °C), 21.47% (500 °C), 26.74% (550 °C), 21.43% (600 °C) (Fig. 2c). Combined with its superior catalytic performance, PA was chosen for subsequent carbonization parameter optimization.

As shown in Fig. 2d, e, the initial decomposition temperatures (T_{onset}) and T_{max} of PA/DJ were gradually decreased with increasing PA concentration (10–30 wt%). Higher concentrations (up to 30 wt%) reduced sheet resistance of carbonized fabrics (Fig. 2f), but 30 wt% PA caused unacceptable brittleness before and after carbonization (Supplementary Video S1), consistent with phosphorus overloading in cellulosic materials[48], thus 25 wt% was optimal. Carbonization temperature studies (400–600 °C) showed PA/DJ achieved excellent conductivity at lower temperatures. At 500 °C, its sheet resistance was 8.48 ± 0.45 Ω/sq (Fig. 2g), meeting sensor application requirements[49,50], untreated DJ needed 700 °C for comparable conductivity (Fig. 2h), confirming PA reduces carbonization temperature by 200 °C. Dwell time optimization at 500 °C (10–60 min) showed sheet resistance stabilized after 40 min (8.48 ± 0.45 Ω/sq), with little change at longer durations (8.72 ± 0.40 Ω/sq at 50 min; 8.29 ± 0.24 Ω/sq at 60 min) (Fig. 2i). Considering energy efficiency, 40 min was selected as optimal, supporting sustainable manufacturing[31]. As shown in Supplementary Table

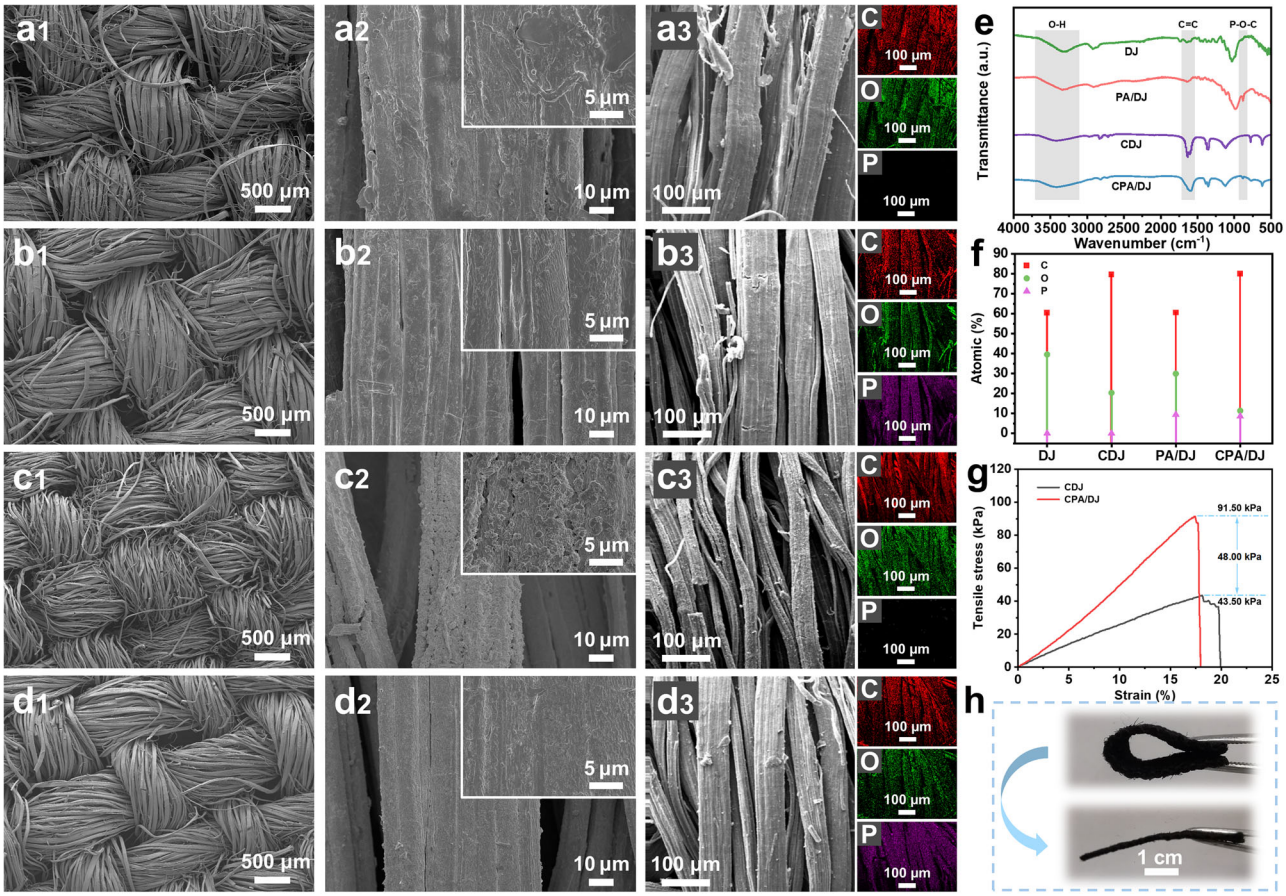

Fig. 3 | Characterization of morphology and mechanical properties of carbonized jute fabric. SEM images of **a**1 DJ, **b**1 PA/DJ, **c**1 CDJ, and **d**1 CPA/DJ at 50×, and the corresponding SEM images with higher magnifications at 1000× **a**2, **b**2, **c**2, **d**2 and 5000× (inset on the top right), EDS images of **a**3 DJ, **b**3 PA/DJ, **c**3 CDJ, **d**3 CPA/DJ. **e** FTIR spectra of of DJ, PA/DJ, CDJ and CPA/DJ. **f** Distribution of surface elements on fabric. **g** Stress-strain curves for CDJ and CPA/DJ. **h** Bending and recovery diagram for CPA/DJ.

S1, sensors prepared using carbonized biomass exhibited carbonization temperatures around 800 °C and required extended

carbonization times, resulting in higher energy consumption. The aforementioned findings demonstrate that this research has made significant contributions towards energy conservation.

Structural and mechanical characterization of carbonized jute fabrics

The surface morphologies of DJ, carbonized degummed jute fabric (CDJ), PA/DJ and CPA/DJ were characterized using scanning electron microscopy (SEM), with comparative mechanical properties of carbonized fabrics quantitatively analyzed. Macrostructural analysis revealed distinct pathways of structural evolution (Fig. 3a1–d3). Minimal morphological differences were observed between DJ and PA/DJ (Fig. 3a1, b1), indicating homogeneous deposition of PA on jute fibers. After carbonization, both fabrics shrank dimensionally. CDJ, however, developed a porous and loosely

packed structure (Fig. 3c1) due to uncontrolled pyrolysis[51]. In contrast, CPA/DJ maintained a denser, more compact architecture with less pronounced shrinkage (Fig. 3d1), a result of the more homogeneous carbonization catalyzed by PA. Microstructural examination showed that CDJ fibers were finer and more fragmented, with pronounced cracking (Fig. 3c2). In contrast, CPA/DJ maintained a smooth, aggregated surface with minimal structural distortion (Fig. 3d2). This stability arises from PA's acidic nature and its thermal decomposition products (e.g., pyrophosphoric acid and phosphoric acid), which catalyze dehydration and promote the formation of a dense surface char layer, enhancing carbon retention and structural integrity at elevated temperatures[41].

To clarify how PA treatment improves jute carbonization, the macroscopic morphology of four sample sets (DJ, PA/DJ, CDJ, CPA/DJ) was analyzed using 3D optical microscopy[52]. The carbonized samples showed distinct area shrinkage: CDJ shrank by 41.42% ±2.1%, versus 13.48% ±0.8% for CPA/DJ (Supplementary Fig. S3). Fiber diameter shrinkage followed a similar trend: 21.84% ±1.5% for CDJ compared to 7.22% ±0.6% for CPA/DJ (Supplementary Fig. S4).

Thickness measurements further revealed distinct final thicknesses: DJ (1.18 ± 0.5 mm), PA/DJ (1.20 ± 0.6 mm), CDJ (0.77 ± 0.01 mm), and CPA/DJ (0.98 ± 0.02 mm) (Supplementary Fig. S5). Morphologically, CDJ fibers showed scattered, uneven yellowish spots (Supplementary Fig. S3b), while CPA/DJ exhibited a glossy, homogeneous black surface (Supplementary Fig. S3d), suggesting that PA promotes more complete carbonization at 500 °C. Collectively, these results confirm that PA treatment markedly reduces dimensional shrinkage during carbonization, preserving the fabric's internal structure for a more uniform and controlled process[53].

Energy-dispersive X-ray spectroscopy (EDS) mapping confirmed the uniform distribution of phosphorus in PA/DJ (Fig. 3b3), verifying successful PA incorporation. Carbonization significantly altered elemental composition in both PA-treated and untreated fabrics: (1) Carbon content increased from 60.59 at% (PA/DJ) to 80.06 at%

(CPA/DJ) and 60.44 at% (DJ) to 79.69 at% (CDJ). (2) Oxygen content decreased from 29.95 at% (PA/DJ) to 11.33 at% (CPA/DJ) and 39.56 at% (DJ) to 20.31 at% (CDJ), consistent with enhanced carbonization efficiency in PA-treated samples[54]. The compact morphology of CPA/DJ suggests superior mechanical retention compared to CDJ, while the conductive carbon network formed during PA-assisted carbonization imparts electrical

functionality[55]. These findings align with prior studies on acid- catalyzed carbonization in cellulosic materials[56].

Fourier-transform infrared (FTIR) analysis (Fig. 3e) investigated the chemical interaction between PA and jute fabric. The presence of a characteristic peak at 878 cm^{-1} in both PA/DJ and CPA/DJ spectra, attributed to P–O–C stretching vibrations[36,57], confirms the successful covalent incorporation of PA into the cellulose matrix.

Carbonization induced notable spectral changes: the decreased intensity of the 878 cm^{-1} peak in CPA/DJ suggests partial loss of phosphorus-containing groups[58], while enhanced C=C stretching vibrations (1720–1540 cm^{-1}) indicate progressive aromatization[59], The reduction in O–H stretching intensity (3050–3700 cm^{-1}) further supports dehydration during thermal treatment[57].

X-ray photoelectron spectroscopy (XPS) was used to determine the chemical states of constituent elements. The survey spectra (Supplementary Fig. S6a) show dominant C_{1s} and O_{1s} peaks for both DJ and PA/DJ, with a new P_{2p} peak appearing in the latter. High-resolution spectra (Supplementary Fig. S6b–f) confirm the chemical grafting of PA onto cellulose: the C_{1s} spectrum shows a new peak at 286.8 eV assigned to C–O–P[41]; the O_{1s} spectrum exhibits new peaks at 532.1 eV (C–O–P) and 531.0 eV (P=O)[35,41]; and the P_{2p} spectrum shows characteristic peaks at 133.1 eV (P–O) and 132.3 eV (P=O)[60–62]. These results collectively demonstrate the stable presence of phosphorus primarily in C–O–P and P–O/P=O configurations, confirming successful phosphate ester bond formation, consistent with FT-IR findings.

After carbonization, the survey spectra of CDJ and CPA/DJ (Supplementary Fig. S7a) show similar patterns, but with a significantly stronger C_{1s} peak and a weaker O_{1s} peak in CPA/DJ, indicating a higher degree of carbonization. The P_{2p} signal remains detectable. High-resolution C_{1s} spectra (Supplementary Fig. S7b, d) reveal a markedly higher C–C peak intensity in CPA/DJ and a new peak at 288.1 eV attributed to C–O–P[41,60,63], confirming that PA treatment enhances carbonization efficiency while retaining phosphorus. The O_{1s} spectra (Supplementary Fig. S7c, e) of CPA/DJ show characteristic peaks for P=O (531.1 eV) and C–O–P (532.3 eV)[35,64], and the P_{2p} spectrum (Supplementary Fig. S7f) confirms the persistence of P–O and P=O bonds. These results demonstrate that C–O–P, P–O, and P=O configurations are preserved post-carbonization, consistent with FT-IR analysis.

Furthermore, CPA/DJ exhibited a maximum tensile strength of 91.50 ± 3.10 kPa, a 2.1-fold increase over CDJ (43.52 ± 2.80 kPa) under identical carbonization conditions (500 °C, Fig. 3g). The material also demonstrated excellent flexibility, fully recovering its shape after 180° bending (Fig. 3h). These mechanical properties, together with its electrical conductivity, confirm that PA treatment promotes a dense and structurally integrated yet flexible carbon layer, which is essential for advanced sensor applications. The comprehensive enhancement in properties achieved through PA modification provides a strong foundation for developing high-performance flexible electronics.

The graphitization degree of carbonized fabrics was systematically characterized using X-ray diffraction (XRD) (Fig. 4a) and Raman spectroscopy (Fig. 4b, c). As shown in Fig. 4a, carbonized samples exhibit a distinct diffraction peak at $2\theta = 24°$, corresponding to the (002) crystal plane of graphitic structures, which is characteristic of amorphous carbon and disordered graphite[59,65]. The intensity of this peak reflects both the interlayer spacing of carbon sheets and the overall crystallinity of the material. Additionally, a broad, less prominent peak is observed at $2\theta = 44°$, associated with the (100) crystal plane of graphite, whose intensity correlates with the in-plane ordering of graphite microcrystals[59,65]. For fabrics carbonized at 500 °C the XRD pattern shows a prominent (002) peak near 24° alongside a discernible yet broad feature around 44°, indicative of turbostratic carbon. These observations suggest the emergence of in-plane ordering, although with notably lower coherence compared to the well-defined interlayer stacking.

Raman spectroscopy further elucidated the graphitization behavior, with carbonized fabrics showing two primary characteristic peaks: the D band at 1360 cm^{-1} (attributed to defective or disordered carbon structures) and the G band at 1580 cm^{-1} (corresponding to ordered graphitic carbon)[66]. The graphitization degree was quantitatively assessed using the intensity ratio of these bands (I_D/I_G)[66]. As depicted in Fig. 4b, Raman analysis of CPA/DJ samples carbonized at different temperatures revealed a progressive increase in graphitization degree with rising carbonization temperature, as evidenced by decreasing I_D/I_G values. Specifically, Fig. 4c shows that jute fabric without PA treatment required carbonization at 700 °C to achieve an I_D/I_G ratio of 0.82, whereas PA-treated fabric (CPA/DJ) reached a comparable I_D/I_G ratio of 0.83 at only 500 °C (Fig. 4b). This striking similarity in graphitization degree at a 200 °C lower temperature directly confirms the efficacy of PA treatment in reducing the carbonization temperature while maintaining structural quality.

The mechanical properties of carbonized jute fabrics exhibited strong temperature dependence, as revealed by systematic characterization (Fig. 4d, e). CDJ showed a dramatic 40.40% reduction in fracture strength (from 6.51 to 3.88 kPa) between 600 and 650 °C, corresponding to the pyrolysis of residual lignin that substantially compromised mechanical integrity[67]. While further temperature increases to 800 °C caused additional strength reductions, the changes were less pronounced as major pyrolysis events were completed by 650 °C (char yield: 10.61 ± 0.7%), with subsequent heating mainly exacerbating brittle behavior (fracture strain decreasing from 12.05% to 8.04%).

In contrast, CPA/DJ demonstrated superior thermal stability, maintaining consistent fracture strength between 400–500 °C (Fig. 4e). However, a sharp 51.07% strength reduction occurred at 550 °C (from 91.50 to 44.77 kPa), establishing 500 °C as the optimal carbonization temperature for balancing mechanical and electrical properties. The non-monotonic variation in elongation at break with temperature is attributed to competing mechanisms: pore development (Supplementary Fig. S8) at elevated temperatures facilitates strain accommodation, while excessive heat compromises structural integrity, diminishing load-bearing capacity[68–70].

To enhance mechanical performance for wearable applications, TPU encapsulation was employed, dramatically improving key properties: Fracture strength increased from 91.50 kPa to 1160.33 kPa, and elongation at break enhanced from 17.96% to 33.73% (Fig. 4f). As shown in Supplementary Fig. S9, cyclic tensile tests were performed on the TPU/CPA/DJ material for 50 cycles at 30% strain. The hysteresis loops exhibited a slight downward shift with increasing cycle numbers, indicating relatively stable cyclic tensile performance of the material. These values meet fundamental requirements for pressure sensor applications[49]. Comparative analysis of four treatment conditions (CDJ-700 °C, CDJ-500 °C, CPA/DJ-500 °C, and TPU/CPA/DJ-500 °C) confirmed progressive improvements in all mechanical parameters (Fig. 4g–i), validating the effectiveness of each processing step.

Performance evaluation of TPU/CPA/DJ flexible pressure sensors

To validate the suitability of CPA/DJ carbonized at 500 °C as a conductive substrate for pressure sensing, we fabricated a flexible piezoresistive pressure sensor via TPU encapsulation, denoted as TPU/CPA/DJ. The sensor's performance including sensitivity, response time, cyclic stability and mechanical robustness (compression resilience) were systematically characterized. The specific optimization process for TPU concentration is illustrated in Supplementary Fig. S10–14, along with their associated descriptions.

The TPU on the outer layer of the sensor forms a relatively uniform film on the surface of the carbonized fabric, while the inner layer of carbonized fabric and the fibers form a network-like support for the TPU (Supplementary Fig. S13), giving the sensor better mechanical and durability properties. As shown in Fig. 5a, the sensitivity curve exhibits three distinct regimes. The four-layer TPU/CPA/DJ flexible pressure sensor exhibited distinct sensitivity regimes across different pressure ranges (Fig. 5a): (1) High-sensitivity region (0–12 kPa): A sensitivity of 5.28 kPa^{-1} was observed, attributed to the rapid formation of conductive pathways during

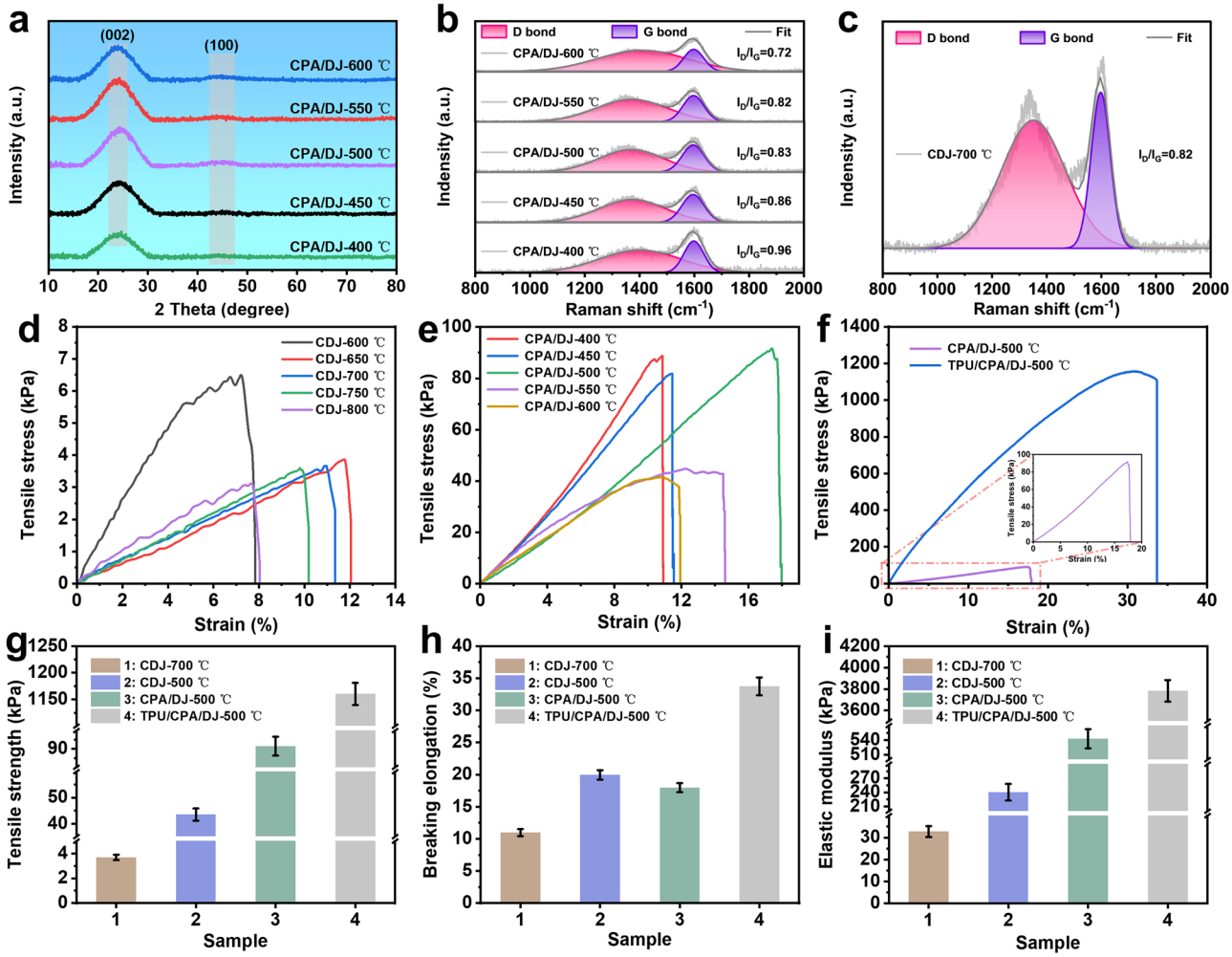

Fig. 4 | Comparison of graphitisation degree and mechanical properties of samples. a XRD patterns of jute fabrics treated with PA-assisted carbonization at different temperatures. **b** Raman spectra of jute fabrics with PA-assisted carbonization at different temperatures. **c** Raman spectra of carbonized jute fabrics at 700 °C. **d** Stress-strain curve of CDJ at 600–800 °C. **e** Stress-strain curves of CPA/DJ at 400–600 °C. **f** Stress-strain curves of carbonized fabric before and after TPU encapsulation. **g** Tensile strength of carbonized jute under different treatment conditions. **h** Carbonized jute elongation at break under different treatment conditions. **i** Modulus of elasticity of carbonized jute under different treatment conditions.

initial contact between the fabric layers and fibers. (2) Intermediate regime (12–90 kPa): Sensitivity decreased to 0.18 kPa^{-1} as the TPU insulating network became compressed, leading to more gradual resistance changes.(3) Saturation regime (90–200 kPa): Further compression yielded minimal sensitivity (0.03 kPa^{-1}), suggesting near-maximum conductive pathway formation[5].

The sensor's performance varies with layer number: sensitivity initially rises then slightly declines (Supplementary Fig. S15), while breaking strength increases progressively (Supplementary Fig. S16). This mechanical enhancement stems from the cumulative TPU network in multi-layer structures, which stabilizes the fabric and mitigates localized fracture (Supplementary Fig. S13)[71–73]. Although stacking improves sensitivity and stability, performance does not increase indefinitely; a six-layer sensor shows poor bendability (Supplementary Fig. S17). A four-layer construct achieves the optimal balance, and its reproducible fabrication is confirmed by consistent sensitivity results from replicate samples (Supplementary Fig. S18).

The sensor maintained excellent linearity across 0–200 kPa (Fig. 5b), conforming to Ohm's law. The increasing slope of the resistance-pressure curve confirmed the expected piezoresistive behavior, where applied pressure reduced inter-fabric contact resistance[74].

The sensor demonstrated rapid response times (198 ms for loading, 87 ms for unloading; Fig. 5c), critical for real-time applications[75]. Cyclic testing under varying pressures (Fig. 5d) and frequencies (0.05–0.5 Hz;Fig. 5e) revealed high repeatability, with signal deviations <2% over five random cycles, confirming stability[5]. Mechanical testing under compressive strains (20–60%) highlighted the sensor's elastic recovery, with minimal plastic deformation even at 60% strain (Fig. 5f). Fatigue resistance was validated through 3000 compression cycles (50% strain; Fig. 5g), where stress-strain curves stabilized after 100 cycles and retained performance thereafter. Long-term stability was further confirmed by 3000 cycles under 0–40 kPa (Fig. 5h), with consistent signal output despite minor initial fluctuations due to mechanical settling[76]. Furthermore, after 3000 cycles of compression, the fibers in the sensor cross-section remained relatively intact (Supplementary Fig. S19). which proves that the sensor has an excellent fatigue resistance and a long service life.

To elucidate the operational mechanism of the TPU/CPA/DJ pressure sensor, we conducted a comprehensive analysis of its electromechanical behavior. Figure 6a presents the equivalent circuit model, where the total system resistance comprises two key components, a relatively constant resistance (R_0) originating from connecting wires and conductive adhesive, and a pressure-dependent variable resistance (R) arising from the sensor's conductive network.

Phase I: multi-scale gap compression (low pressure: 0–12 kPa). At zero load, the sensor features a hierarchical porous structure with

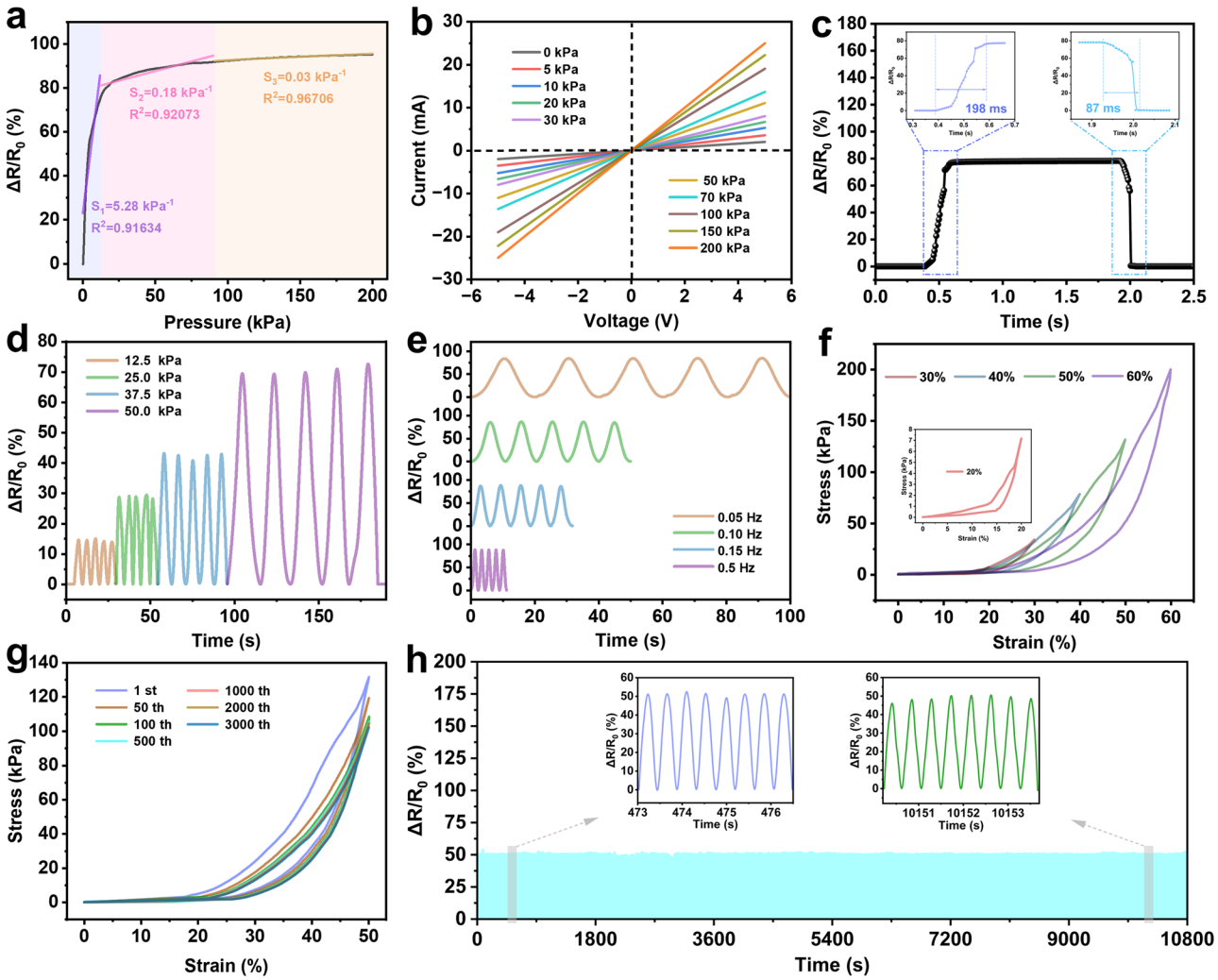

Fig. 5 | Sensing properties of the TPU/CPA/DJ flexible pressure sensors. **a** Sensitivity of TPU/CPA/DJ pressure sensors. **b** *I–V* curves at different applied pressures. **c** Response and recovery times of the sensors in loading and unloading tests. **d** Sensing curves at different loading pressures. **e** Sensing curves at different loading frequencies. **f** Stress-strain curves of sensors under different deformations. **g** Stress-strain curves of sensors under cyclic compression of 3000 cycles at 50% deformation. **h** Signal stability of the sensor subjected to 3000 loading-unloading cycles under a stress of 40 kPa.

insulating voids at three scales: inter-fabric gaps between stacked carbonized layers, inter-fiber voids within each layer, and microporosity within carbonized fibers. Under initial pressure, these compressible voids are preferentially closed through two simultaneous processes: (i) interlayer compression, which rapidly reduces macroscopic gaps and establishes initial contact between adjacent conductive layers; and (ii) intralayer densification, which compresses inter-fiber spaces and increases fiber–fiber contact points[49]. The synergistic closure of these multi-scale voids produces a sharp, nonlinear rise in conductive pathways, accounting for the high initial sensitivity (S_1 = 5.28 kPa^{-1}, Fig. 5a).

Phase II: matrix consolidation & percolation saturation (medium pressure: 12–90 kPa). With increasing pressure, most compressible voids are eliminated. Further reduction in resistance is governed by progressive compression of the TPU insulating matrix and continued consolidation of the fabric layers. The compliant TPU deforms, enhancing interfacial contact at fiber–fiber and layer–layer junctions. As the conductive network approaches its densest packing, the rate of new pathway formation decreases significantly, resulting in a transition to a lower yet stable sensitivity (S_2 = 0.18 kPa^{-1})[77].

Phase III: bulk deformation & saturation (high pressure: 90–200 kPa). At high pressures, the system enters a saturation regime. The dominant mechanisms become compression of the intrinsic pore structure within carbonized fibers and bulk deformation of the densely packed composite. Minor resistance decreases arise from fiber surface flattening and maximized interfacial contact area. These changes require substantial additional force, yielding minimal sensitivity (S_3 = 0.03 kPa^{-1}), consistent with piezoresistive saturation behavior in such composites[78].

To evaluate the practical performance of the TPU/CPA/DJ flexible pressure sensors, we systematically tested their response across an extensive pressure range (Pa to hundreds of kPa), demonstrating versatile real-world applicability.

As shown in Fig. 7a, the sensor exhibited distinct and reproducible signal patterns when subjected to airflow perturbations from an earwash ball (Pa-range stimuli), confirming its capability for subtle environmental monitoring. The detection threshold was further verified through controlled tests with ultralight objects including a 0.5 g curved pin (Fig. 7b) and a 5 g A4 paper sheet (1 cm^2 contact area, Fig. 7c). In both cases, the sensor generated clearly differentiable signal magnitudes corresponding to the applied masses, suggesting potential for precise mass discrimination in micro-load applications.

For biomechanical applications, sensors were securely attached to anatomical joints (wrist, elbow, knee) using medical-grade polyurethane hypoallergenic adhesive (Fig. 7d–f). The devices reliably tracked repetitive bending motions, with signal patterns accurately reflecting joint kinematics.

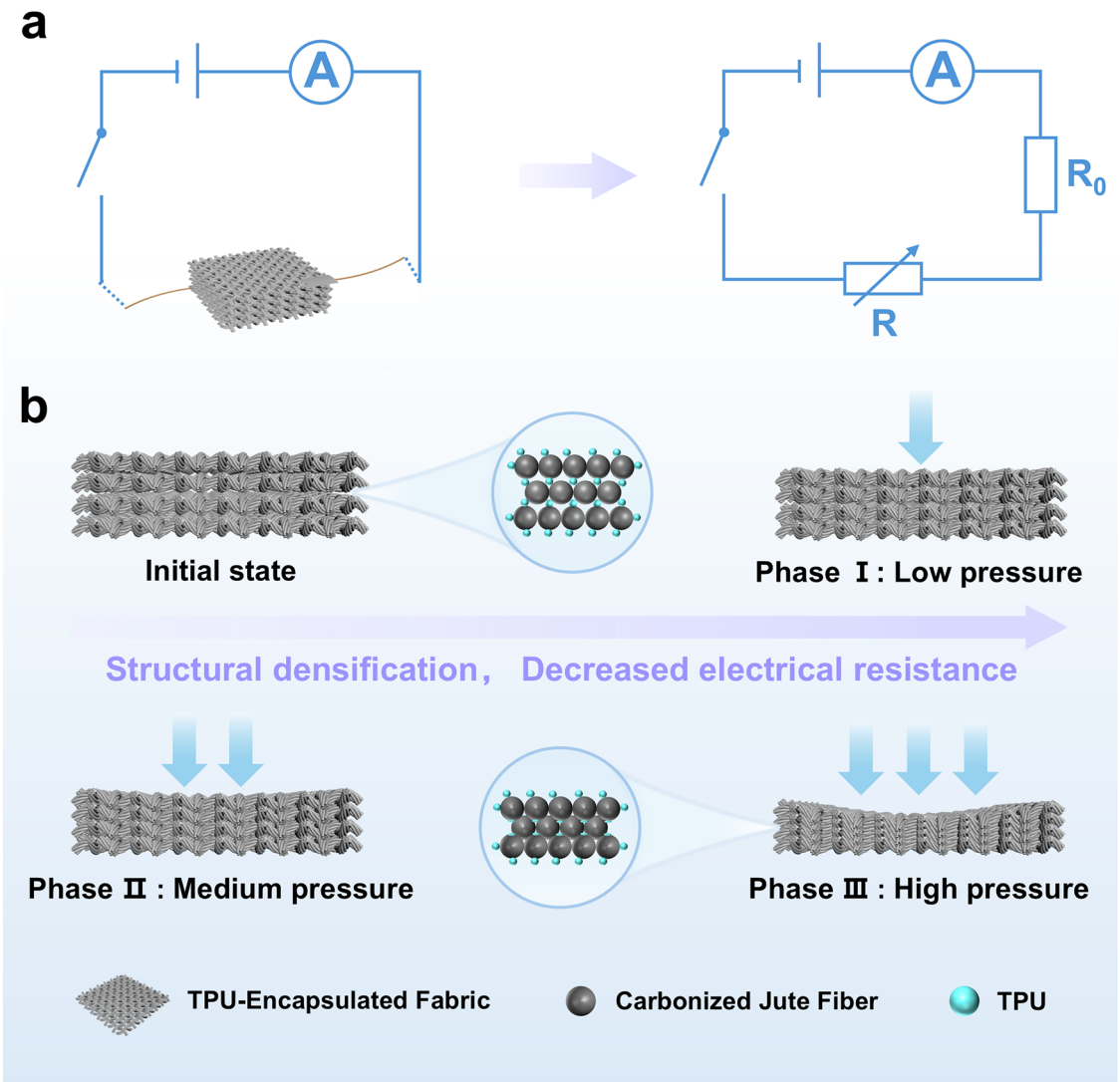

Fig. 6 | Operating mechanism of TPU/CPA/DJ flexible pressure sensor. a Equivalent circuit of the sensor. **b** Schematic diagram of the principle of sensor loading process.

This performance meets essential requirements for wearable motion sensing[79].

A five-sensor array integrated across finger joints (Fig. 7g) successfully distinguished between different hand gestures through characteristic response patterns. Furthermore, the system demonstrated capability for symbolic communication by generating Morse code signals for letters "D", "H", and "U" (Fig. 7h) through timed finger presses[80]. This implementation highlights the sensor's potential for prosthetic control interfaces, silent communication systems and augmented reality input devices.

Discussion

This study demonstrates an innovative flame-retardant-assisted low-temperature carbonization strategy for jute fabrics using PA as a catalytic reagent. The treatment reduces the carbonization temperature by 200 °C while substantially enhancing mechanical properties, tensile strength increases from 3.68 kPa to 91.50 kPa and elongation at break improves from 10.97% to 17.96%. This approach effectively lowers energy consumption and mitigates the intrinsic brittleness of carbonized natural fibers. The carbonized jute fabric was encapsulated with TPU to fabricate a flexible pressure sensor. The resulting TPU/CPA/DJ sensor exhibits high sensitivity (5.28 kPa^{-1}), a wide detection range (5 Pa to 200 kPa), rapid response/recovery (198/87 ms), and excellent cycling stability (3000 cycles). It successfully monitors both human motion and subtle environmental stimuli, indicating strong potential for wearable and environmental sensing applications.This strategy opens a viable pathway for the scalable fabrication of high-performance biomass-derived sensors, supporting the advancement of sustainable flexible electronics.

Methods

Materials

Coarse jute fabric (70#) was supplied by Shandong Yingjie Textile Co., Ltd. Sodium hydroxide (NaOH) was provided by Sinopharm Chemical Reagent Co., Ltd. Phytic acid ($C_6H_{18}O_{24}P_6$) and aluminum hypophosphite ($Al(H_2PO_2)_3$) were obtained from Shanghai Titan Scientific Co., Ltd. Ammonium polyphosphate (APP) was sourced from Shanghai Yuanye Bio-Technology Co., Ltd. Thermoplastic polyurethane (TPU) was acquired from Jiangsu Zhongcai Sifu New Material Co., Ltd. N,N-dimethylformamide (DMF) was procured from Shanghai YiEn Chemical Technology Co., Ltd.

Jute degumming treatment

Jute fabric was treated in 10 wt% NaOH solution at 95 °C for 3 h under reflux. Following treatment, the fabric underwent continuous rinsing until neutral pH was achieved, then oven-dried at 60 °C to obtain DJ.

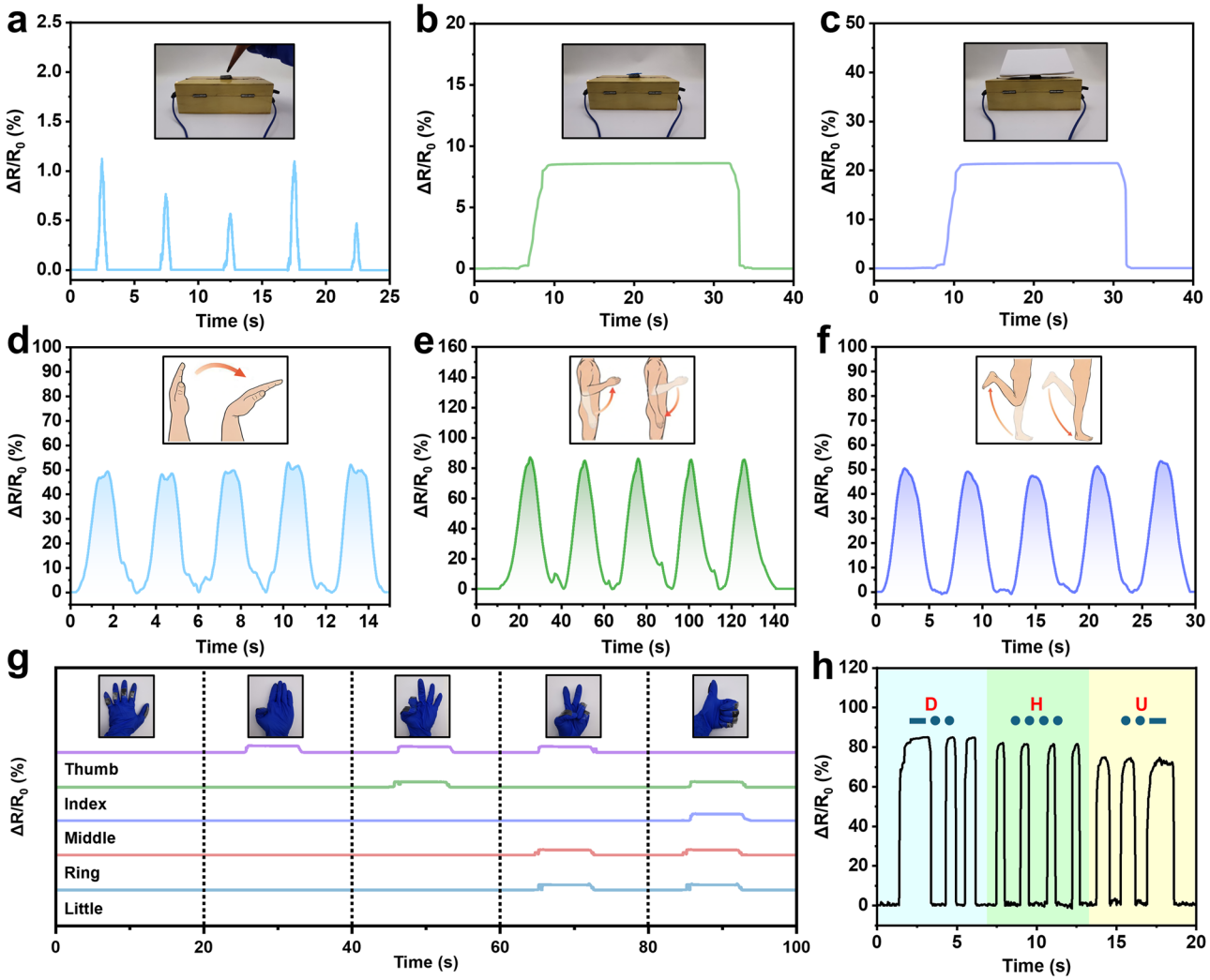

Fig. 7 | Application demonstration of TPU/CPA/DJ flexible pressure sensors. **a** Response curve of TPU/CPA/DJ flexible pressure sensor when airflow blowing, **b** curved pin placement, and **c** A4 paper placement. **d** Response curve of TPU/CPA/DJ flexible pressure sensor during wrist flexion, **e** elbow flexion, and **f** knee flexion. **g** Response curve of TPU/CPA/DJ flexible pressure sensor under different hand gestures. **h** Finger pressing TPU/CPA/DJ flexible pressure sensor outputs the letters "D", "H" and "U" in Morse code.

Preparation of carbonized fabric

DJ fabric was immersed in 25 wt% PA solution for 10 min, followed by padding at 80% pick-up rate. The fabric was subsequently cured at 120 °C for 5 min and oven-dried at 60 °C to obtain PA/DJ. The fabric was then pre-oxidized in a tube furnace by heating to 200 °C at 2 °C/min with a 1 h isothermal hold. Subsequent carbonization under nitrogen atmosphere proceeded at 500 °C for 1 h (heating rate: 5 °C/min), yielding CPA/DJ.

Sensor fabrication

A TPU solution was prepared by dissolving 1 g TPU in 10 g N,N-dimethylformamide (DMF) with stirring at 80 °C for 1 h. Carbonized fabric stacks (four-layer assembly) were immersed in the solution for 10 min and subsequently retrieved. Samples were transferred into deionized water, inducing TPU deposition onto carbonized fabric surfaces via non-solvent induced phase separation (NIPS). This yielded a four-layer pressure sensor (TPU/CPA/DJ).

Characterization

Surface morphology was characterized using an ultra-high-resolution field emission scanning electron microscope (FE-SEM, Hitachi Regulus 8100, Japan) operated at an accelerating voltage of 5 kV. Structural characteristics were analyzed by X-ray diffraction (XRD, Rigaku Ultima IV, Japan) with diffraction angles scanned over a 2θ range of 5° to 90°. The electrical square resistance of the carbonized jute fabric was tested using the RTS-9 four-probe resistance tester (Suzhou Jingge Electronic Co., Ltd). Thermal stability was evaluated by thermogravimetric analysis (TGA, Netzsch TG 209 F3, Germany) under nitrogen atmosphere, with temperature ramping from 30 to 900 °C at a heating rate of 10 °C/min. Structural characterization of carbonized fabrics was performed using confocal Raman microscopy (Renishaw inVia Reflex, UK) with a 532 nm laser under conventional measurement conditions. Samples were analyzed for water contact angle (DSA30, Krüss, Germany) to assess the wettability. Chemical structural evolution of jute fabric before and after carbonization was characterized by Fourier transform infrared spectroscopy (FTIR, Thermo Scientific Nicolet iS10) over the wavenumber range of 650–4000 cm^{-1} at 4 cm^{-1} resolution. The elemental composition and chemical states were analyzed using X-ray photoelectron spectroscopy (XPS,Thermo ESCALAB 250XI). Characterization of fabric morphology using a super-depth-of-field three-dimensional microscope (VHX-6000). The electrochemical properties of the samples were measured on electrochemical workstation (CHI660E, Shanghai Chenhua). Mechanical properties were measured using a universal testing machine (HONGyan HY 940F, China) according to ASTM D638 at a crosshead speed of 5 mm/min. Resistance variation as a function of strain was monitored in real-time using a digital multimeter (DMM 6500, Keithley, USA).

The sensitivity of the sensor is denoted by S and is calculated according to the following equation Eq. (1):

$$S = \frac{(\Delta R/R_0)}{\Delta P} \times 100\% \quad (1)$$

where R_0 denotes the initial resistance of the sensor when no pressure is applied, ΔR denotes the difference between the resistance and R_0 after pressure is applied, and ΔP denotes the amount of change in pressure.

The carbon yield was calculated according to the formula Eq. (2):

$$\text{carbon yield} = \frac{W_b}{W_a} \times 100\% \quad (2)$$

Where W_a is the mass of the sample before carbonization measured after vacuum drying and W_b is the mass of the sample measured after carbonization and drying.

Data availability

The datasets generated and/or analyzed during the current study are not publicly available due to containing information that could compromise the commercial application and potential patent filing, but are available from the corresponding author on reasonable request.

Received: 15 September 2025; Accepted: 22 January 2026;
Published online: 05 February 2026

References

1. Meng, K. et al. Wearable pressure sensors for pulse wave monitoring. *Adv. Mater.* **34**, e2109357 (2022).
2. Yang, J. et al. Self-spiking linear neuromorphic soft pressure sensor for underwater sensing applications. *Adv. Mater.*, e05486, https://doi.org/10.1002/adma.202505486 (2025).
3. Tang, C. et al. Ultrasensitive textile strain sensors redefine wearable silent speech interfaces with high machine learning efficiency. *npj Flex. Electron*. **8** https://doi.org/10.1038/s41528-024-00315-1 (2024).
4. Vaghasiya, J. et al. Wearable sensors for telehealth based on emerging materials and nanoarchitectonics. *npj Flex. Electron* **7**, 26 (2023).
5. Zheng, B. et al. Blade-coated porous 3D carbon composite electrodes coupled with multiscale interfaces for highly sensitive all-paper pressure sensors. *Nano Micro Lett*. **16** https://doi.org/10.1007/s40820-024-01488-0 (2024).
6. Yang, Y. et al. Programmable and scalable embroidery textile resistive pressure sensors for integrated multifunctional smart wearable systems. *Adv. Fiber Mater.* **7**, 574–586 (2025).
7. Pu, J. et al. Dual-dielectric-layer-based iontronic pressure sensor coupling ultrahigh sensitivity and wide-range detection for temperature/pressure dual-mode sensing. *Adv. Mater*. e03926 https://doi.org/10.1002/adma.202503926 (2025).
8. Jin, Y. et al. Flexible pressure sensors enhanced by 3D-printed microstructures. *Adv. Mater.* **37**, e2500076 (2025).
9. Zhao, Y. et al. Eco-friendly multifunctional hydrogel sensors enabled sustainable and accurate human-machine interaction system. *Adv. Mater*. e2507127, https://doi.org/10.1002/adma.202507127 (2025).
10. Tian, X. et al. A fully-integrated flexible in-sensor computing circuit based on gel-gated organic electrochemical transistors. *npj Flex. Electron*. **9**, https://doi.org/10.1038/s41528-025-00472-x (2025).
11. Xu, C. et al. Flexible pressure sensors in human–machine interface applications. *Small* **20**, https://doi.org/10.1002/smll.202306655 (2023).
12. Nie, Z. et al. Mechanically active materials and devices for bio-interfaced pressure sensors-a review. *Adv. Mater.* **36**, e2205609 (2024).
13. Zhang, X. et al. Facile preparation of porous MXene/cellulose nanofiber composite for highly-sensitive flexible piezoresistive sensors in e-skin. *Chem. Eng. J*. **505**, https://doi.org/10.1016/j.cej.2025.159369 (2025).
14. Wang, M. et al. High-performance flexible pressure sensor based on synergistic enhancement of magnetic field oriented carbon Nanotube/Graphene and microdome array structure. *Chem. Eng. J*. **511**, https://doi.org/10.1016/j.cej.2025.162053 (2025).
15. Lin, K. et al. Island-bridge microcracks with nanofiber and carbon nanotube composites for high-performance flexible strain sensors. *Compos. Part B Eng*. **298**, https://doi.org/10.1016/j.compositesb.2025.112366 (2025).
16. Wang, M. et al. Highly stable and wide-range flexible pressure sensors with a gradient modulus and selective foaming layer. *Chem. Eng. J*. **515**, https://doi.org/10.1016/j.cej.2025.163761 (2025).
17. Chen, Z. et al. Fibrous pressure sensor with unique resistance increase under partial compression: coaxial wet-spun TiO(2)/graphene/thermoplastic polyurethane multi-wall multifunctional fiber. *Adv. Mater.* e2509631 https://doi.org/10.1002/adma.202509631 (2025).
18. Meng, J. et al. Schottky-contacted nanowire sensors. *Adv. Mater.* **32**, e2000130 (2020).
19. Guan, M. et al. Gold nanoparticles incorporated liquid metal for wearable sensors and wound healing. *Chem. Eng. J*. **508**, https://doi.org/10.1016/j.cej.2025.161120 (2025).
20. Zhou, Y. et al. Ionic composite nanofiber membrane-based ultra-sensitive and anti-interference flexible pressure sensors for intelligent sign language recognition. *Adv. Funct. Mater*. **35**, https://doi.org/10.1002/adfm.202425586 (2025).
21. Chen, Y. et al. Ultra-high filling ratio of non-percolative rapeseed-shaped liquid metal fiber mats for pressure sensors via electrospinning aided inhomogeneous dispersion. *Adv. Fiber Mater.* **7**, 633–644 (2025).
22. Wang, W. et al. Synergistic enhancement of hole–bridge structure and molecular-crowding effect in multifunctional eutectic hydrogel strain/pressure sensor for personal rehabilitation training. *Adv. Funct. Mater*. https://doi.org/10.1002/adfm.202502844 (2025).
23. Su, X. et al. Rapid and controllable preparation of multifunctional lignin-based eutectogels for the design of high-performance flexible sensors. *ACS Appl. Mater. Interfaces* **15**, 45526–45535 (2023).
24. Li, Y. et al. An ultrastretchable and multifunctional hydrophobic/electrostatic dual-crosslinked hydrogel for self-healing flexible touch panel and sensor. *npj Flex. Electron*. **9** https://doi.org/10.1038/s41528-025-00422-7 (2025).
25. Tian, R. et al. Exceptional recognition of ammonia in gas-sensing applications: Constructing sensitive 0D/3D heterojunctions of ZnO nanoparticles/ZnSnO3 hollow cubes and density functional theory analysis. *Chem. Eng. J*. **519**, https://doi.org/10.1016/j.cej.2025.165394 (2025).
26. Liu, J. et al. Correction: durable Fe_3O_4/PPy particle flow spun textile for electromagnetic interference shielding and joule heating. *Adv. Fiber Mater*. **7**, 2064 (2025).
27. Wang, W. et al. Insight into SnO_2-based gas-sensitive materials and readout circuits for semiconductor gas sensors. *Nano Mater. Sci*. https://doi.org/10.1016/j.nanoms.2024.10.012 (2025).
28. Wang, H. et al. Advances in carbon-based resistance strain sensors. *ACS Appl. Electron. Mater.* **5**, 674–689 (2023).
29. Alqaderi, A. et al. Carbon-based flexible strain sensors: Recent advances and performance insights in human motion detection. *Chem. Eng. J*. **513**, https://doi.org/10.1016/j.cej.2025.162609 (2025).
30. Shi, L. et al. Applications of carbon-based multivariable chemical sensors for analyte recognition. *Nano Micro Lett.* **17**, 246 (2025).
31. Jin, J. et al. Biopolymer-derived carbon materials for wearable electronics. *Adv. Mater.* **37**, e2414620 (2025).
32. Lam, D. et al. Turning cotton into tough energy textile via metal oxide assisted carbonization. *Carbon* **153**, 257–264 (2019).

33. Zhou, X. et al. From waste cotton linter: a renewable environment-friendly biomass based carbon fibers preparation. *ACS Sustain. Chem. Eng.* **4**, 5585–5593 (2016).
34. Liu, S. et al. Low temperature carbonization and synergistic flame retardancy of cotton fabric coated by phosphorus-nitrogen flame retardants. *Int. J. Biol. Macromol*. **278**, https://doi.org/10.1016/j.ijbiomac.2024.134873 (2024).
35. Song, W. et al. The fabrication of flame-retardant viscose fabrics with phytic acid-based flame retardants: Balancing efficient flame retardancy and tensile strength. *Int. J. Biol. Macromol*. **260**, https://doi.org/10.1016/j.ijbiomac.2024.129596 (2024).
36. Hou, F. et al. A self-assembled bio-based coating with phytic acid and DL-arginine used for a flame-retardant and antibacterial cellulose fabric. *Prog. Org. Coat*. **173**, https://doi.org/10.1016/j.porgcoat.2022.107179 (2022).
37. Rombaldo, C. et al. Brazilian natural fiber (jute) as raw material for activated carbon production. *Acad. Bras. Cienc.* **86**, 2137–2144 (2014).
38. Abit, K. et al. Activated carbons from miscanthus straw for cleaning water bodies in Kazakhstan. *Eurasian Chem. Technol. J*. **21**, https://doi.org/10.18321/ectj867 (2019).
39. Zhang, M. et al. Multi-layered gradient-structured TPU/CNTs aerogel with ultra-wide pressure detection capabilities for machine learning–assisted fruit recognition. *Adv. Compos. Hybrid Mater*. **8**, https://doi.org/10.1007/s42114-024-01157-1 (2024).
40. He, Y. et al. Lightweight, ultra-compressed, and environmentally friendly wood/TPU aerogel sensor based on optimized performance of dynamic 3D pore structure. *J. Colloid Interface Sci.* **678**, 188–199 (2025).
41. Khodavandegar, S. et al. Phytic acid derivatized lignin as a thermally stable and flame retardant material. *Green. Chem.* **26**, 10070–10086 (2024).
42. Gan, J. et al. Lignocellulosic biomass-based carbon dots: synthesis processes, properties, and applications. *Small* **19**, e2304066 (2023).
43. Fan, S. et al. Synthesis of novel high-performance all-biobased wood flame retardant materials using phytic acid and β-cyclodextrin. *Constr. Build. Mater*. **489**, https://doi.org/10.1016/j.conbuildmat.2025.140657 (2025).
44. Tuble, K. A. Q. et al. Synergistic effect of phytic acid and eggshell bio-fillers on the dual-phase fire-retardancy of intumescent coatings applied on cellulosic substrates. *Chemosphere* **358**, 142226 (2024).
45. Wang, B. et al. A higher durability flame retardant for regenerated cellulose fabrics based on fully bio-based phytic acid and L-arginine. *Int. J. Biol. Macromol.* **308**, 142377 (2025).
46. Xu, J. et al. Synergistic flame retardant effect of carbon nanohorns and ammonium polyphosphate as a novel flame retardant system for cotton fabrics. *Chem. Eng. J*. **451**, https://doi.org/10.1016/j.cej.2022.138566 (2023).
47. Wang, Y. et al. A novel iron ion cross-linking strategy dramatically improves the strength and flame retardant of degradable foams from rice straw fibers. *Adv. Compos. Hybrid Mater*. **8**, https://doi.org/10.1007/s42114-024-01082-3 (2024).
48. Orzan, E. et al. Elucidation of cellulose phosphorylation with phytic acid. *Ind. Crops Prod*. **218**, https://doi.org/10.1016/j.indcrop.2024.118858 (2024).
49. Zhang, L. et al. Carbonized cotton fabric-based multilayer piezoresistive pressure sensors. *Cellulose* **26**, 5001–5014 (2019).
50. Barua, A. et al. Biomimetic freestanding microfractals for flexible electronics. *npj Flex. Electron*. **9**, https://doi.org/10.1038/s41528-025-00381-z (2025).
51. Li, C. et al. Sustainable production of porous carbon from biomass: Influence of pre-carbonization on pore evolution and environment impact. *Chem. Eng. J*. **480**, https://doi.org/10.1016/j.cej.2023.148176 (2024).
52. Chen, M. et al. Boosting sensitivity of cellulose pressure sensor via hierarchically porous structure. *Nano Micro Lett.* **17**, 205 (2025).
53. Lee, S. et al. High electrical and thermal conductivities of a PAN-based carbon fiber via boron-assisted catalytic graphitization. *Carbon* **199**, 70–79 (2022).
54. Yue, H. et al. Flame-retardant and form-stable phase-change composites based on phytic acid/ZnO-decorated surface-carbonized delignified wood with superior solar-thermal conversion efficiency and improved thermal conductivity. *ACS Appl. Mater. Interfaces* **15**, 8093–8104 (2023).
55. Egun, I. L. et al. Molten base carbonisation and activation of non-lignin-rich biomass into hierarchically porous carbon with surface-rich functionalities for supercapacitor electrodes. *Chem. Eng. J*. **509**, https://doi.org/10.1016/j.cej.2025.161386 (2025).
56. Zhan, J. et al. Phosphoric acid deconstruction of lignocellulose structure enables an ultra-wide plateau capacity in hard carbon anode. *Carbon* **243**, https://doi.org/10.1016/j.carbon.2025.120597 (2025).
57. Franco-Urquiza, E. et al. Mechanical properties of hybrid carbonized plant fibers reinforced bio-based epoxy laminates. *Polymers* **13**, https://doi.org/10.3390/polym13193435 (2021).
58. Tan, J. et al. Carbon nanotube reinforced carbonized cellulose aerogels for enhanced hemostasis and accelerated skin wound healing. *Adv. Funct. Mater*. https://doi.org/10.1002/adfm.202417798 (2025).
59. Guan, H. et al. A low-temperature carbonization strategy for efficient viscous crude oil spill disposal without hydrophobic coating: CoFe-PBA-catalyzed carbonization of superhydrophobic flame retardant melamine sponge. *Adv. Funct. Mater*. **34**, https://doi.org/10.1002/adfm.202313224 (2023).
60. Song, W. et al. High-efficient flame-retardant finishing of cotton fabrics based on phytic acid. *Int. J. Mol. Sci.* **24**, https://doi.org/10.3390/ijms24021093 (2023).
61. Li, Y. -y et al. Acidity regulation of boron phosphate flame retardant and its catalyzing carbonization mechanism in epoxy resin. *J. Therm. Anal. Calorim.* **129**, 1481–1494 (2017).
62. Wang, D. et al. A bio-based flame-retardant starch based on phytic acid. *ACS Sustain. Chem. Eng.* **8**, 10265–10274 (2020).
63. Mu, Y. et al. Electron acceptor-driven solid electrolyte interphases with elevated LiF content for 4.7 V lithium metal batteries. *Nano Micro Lett.* **17**, 163 (2025).
64. Du, Y. et al. In situ alloying strategy constructed Fe3Co–N–C electrocatalysts with designed 1D/3D hierarchical networks for rechargeable zinc–air battery. *InfoMat* **7**, https://doi.org/10.1002/inf2.70032 (2025).
65. Liu, X. et al. Pore structure design engineering: one-step synthesis of high-performance hard carbon materials with abundant closed pores. *Chem. Eng. J*. **510**, https://doi.org/10.1016/j.cej.2025.161689 (2025).
66. Li, Z. et al. Raman spectroscopy of carbon materials and their composites: Graphene, nanotubes and fibres. *Prog. Mater Sci*. **135**, https://doi.org/10.1016/j.pmatsci.2023.101089 (2023).
67. Upadhyayula, V. K. K. et al. Organosolv lignin carbon fibers and their prospective application in wind turbine blades: An environmental performance assessment. *J. Clean. Prod*. **491**, https://doi.org/10.1016/j.jclepro.2025.144825 (2025).
68. Zhou, W. et al. Bioinspired ultrasensitive flexible strain sensors for real-time wireless detection of liquid leakage. *Nano Micro Lett.* **17**, 68 (2024).
69. Niu, S. et al. Flexible pressure sensor with tunable sensitivity and responsive range for adaptive wearable electronics. *InfoMat* https://doi.org/10.1002/inf2.70059 (2025).
70. Chao, X. et al. Numerical evaluation of the influence of porosity on bending properties of 2D carbon/carbon composites. *Compos. Part B* **136**, 72–80 (2018).

71. Liu, M. et al. Hydrogel-infiltrated micropatterned nano-carbon aerogel sheet composed of partially carbonized cellulose nanofibers for wearable sensor. *Nano Energy* **138**, https://doi.org/10.1016/j.nanoen.2025.110852 (2025).
72. Adibeig, M. et al. Effects of network structure on the viscoelastic creep and delayed fracture of polyelectrolyte elastomers. *Polymer* **305**, https://doi.org/10.1016/j.polymer.2024.127104 (2024).
73. Fuentes del Toro, S. et al. Mechanical performance of 3D-printed TPU auxetic structures for energy absorption applications. *Polym. Test*. **143**, https://doi.org/10.1016/j.polymertesting.2024.108669 (2025).
74. Li, N. et al. Microstructure-modulated linear-response flexible pressure sensors. *Adv. Funct. Mater*. https://doi.org/10.1002/adfm.202509776 (2025).
75. Shi, Z. et al. Morphological engineering of sensing materials for flexible pressure sensors and artificial intelligence applications. *Nano Micro Lett.* **14**, 141 (2022).
76. Yang, M. et al. High-performance flexible pressure sensor with a self-healing function for tactile feedback. *Adv. Sci.* **9**, e2200507 (2022).
77. Wang, X. et al. Highly sensitive ultrathin flexible thermoplastic polyurethane/carbon black fibrous film strain sensor with adjustable scaffold networks. *Nano Micro Lett.* **13**, 64 (2021).
78. Wang, Y. et al. A wearable breathable pressure sensor from metal-organic framework derived nanocomposites for highly sensitive broad-range healthcare monitoring. *Nano Energy* **70**, https://doi.org/10.1016/j.nanoen.2020.104560 (2020).
79. He, T. et al. Toward wearable sensors: advances, trends, and challenges. *ACM Comput. Surv.* **55**, 1–35 (2023).
80. Zhao, X. et al. Flexible pressure sensor based on CNTs/CB/PDMS sponge with porous and microdome structures for sitting posture discrimination. *Chem. Eng. J*. **502**, https://doi.org/10.1016/j.cej.2024.157878 (2024).

Acknowledgements

The research was financially supported by the National Natural Science Foundation of China (No. 22176031) and the National Key R&D Program of China (Grant 2017YFB0309405 and Grant 2017YFB0309100).

Author contributions

Boxuan Zhu: Conceptualization, Methodology, Software, Writing original draft. Lu wen Zhao: Writing – review & editing. Li Lv: Writing – review & editing. Miao Zhang: Supervision, Writing – review & editing. Chengcheng Li: Supervision, Writing – review & editing.: Conceptualization, Methodology. Jie Wang: Validation. Xing Su: Supervision, Writing – review & editing.: Conceptualization, Methodology. Zaisheng Cai: Writing – review & editing, Supervision. Yaping Zhao: Supervision, Writing - review & editing, Project administration, Funding acquisition.

Competing interests

The authors declare no competing interests.

Additional information

Supplementary information The online version contains supplementary material available at https://doi.org/10.1038/s41528-026-00541-9.

Correspondence and requests for materials should be addressed to Ya ping Zhao.